Spatial and temporal distribution of fluvio-morphological processes on a meander point bar during a flood event

Kasvi Elina, Alho Petteri, Vaaja Matti, Hyyppä Hannu and Hyyppä Juha

ABSTRACT

Morphological changes and hydraulic parameters are analyzed over a meander point bar along a sand-bedded river. Morphological changes caused by a flood are mapped using terrestrial and mobile laser scanners. The flow characteristics are simulated over the duration of the flood, which inundated the point bar completely. The spatial distribution of depth-averaged flow velocity, direction, and stream power at two different discharges is analyzed. In addition, the temporal variation of flow velocity, depth, and stream power on the point bar is resolved over the whole inundated period. The changes in discharge control the transverse shift of the high velocity core, which, in turn, has a major impact on the changes over the point bar. For example, a minor decrease in discharge may lead to a notable decrease in flow velocity on the point bar margin, enabling filling. Deposition occurs mainly during the recession of the flood, and thus, the duration of moderate discharges greatly influences accretion. The size of the supplied sediment also influences the filling over the bar head. Erosion mainly takes place during high discharges. A rapid decrease in discharge inhibits chute filling. The latest flood event seems to influence more the erosional compared to depositional processes.

Key words | computational fluid dynamics, mobile laser scanning, morphological change, river bend, terrestrial laser scanning

Kasvi Elina (corresponding author),
Alho Petteri
University of Turku,
Department of Geography and Geology,
FI-20014 Turun Yliopisto,
Finland
E-mail: *emkasv@utu.fi*

Vaaja Matti
Hyyppä Hannu
Alho Petteri
Aalto University,
School of Science and Technology,
Department of Surveying, P.O. BOX 14100,
00076 Aalto,
Finland

Hyyppä Hannu
Helsinki Metropolia University of Applied Sciences,
P.O. BOX 00079,
Metropolia, Helsinki,
Finland

Hyyppä Juha
Finnish Geodetic Institute,
Department of Remote Sensing and Photogrammetry, P.O. BOX 15,
02431 Masala,
Finland

INTRODUCTION

A meandering stream pattern is common in nature and it forms on gentler slopes than braiding (Leopold & Wolman 1957; Smith 1998) and under potential specific stream power below 40 W m^{-2} in sandy rivers (van den Berg 1995). Meandering behavior has been noted to be predictable to some degree (e.g. Thompson 1986), but recent studies claim that local factors play an important role in controlling the morphological changes of a river bend (e.g. Gautier *et al.* 2010; Hooke & Yorke 2011). The inner bank point bar formation affects the flow field, which in turn modifies the point bar, and thus, the consequences of the flow over the point bar depend on the specific fluvio-morphological conditions of the site (e.g. Gautier *et al.* 2010). Hence, the bend and point bar shape is a consequence of local hydraulic factors such as channel slope, flow velocity, depth, stream power, and particle size (e.g. Kleinhans & van den Berg 2011).

Some fluvio-morphological processes, however, have been widely noticed to appear in river bends: during high discharge, the highest stream power is situated near the convex bank at the meander bend entrance, typically causing scour and a high concentration of coarse grain sizes over the point bar head (Bridge & Jarvis 1976; Bluck 1982; Dietrich & Smith 1984; Pyrce & Ashmore 2005). A chute channel may evolve across the point bar platform (Friedkin 1945; McGowen & Garner 1970). The shoaling of the flow over the point bar leads to a decrease in stream power on the point bar platform and tail and to an outward flow over the upstream portion of the point bar (Dietrich & Smith 1983; Ferguson *et al.* 2003; Engel & Rhoads 2012). At the same time, the high velocity core (HVC) shifts laterally towards the concave bank beyond the bend apex due to the combined effect of point bar

doi: 10.2166/nh.2013.091

and bend curvature (Leopold & Wolman 1960; Dietrich & Smith 1983). This leads to secondary circulation of the flow (e.g. Bathurst *et al.* 1979) and a flow separation may occur on the point bar margin (i.e. the concave side of the point bar) (Ferguson *et al.* 2003; Frothingham & Rhoads 2003). As a result, flow velocities over the bar tail become slow, fine material deposits and channel sinuosity increases (Bridge & Jarvis 1976; Pyrce & Ashmore 2005; Alho & Mäkinen 2010). In addition, a scroll bar may form on the point bar margin (Gautier *et al.* 2010; Kleinhans & van den Berg 2011). With lower discharge, the zone of high stream power is located closer to the outer bank at the bend entrance and crosses the channel further upstream (Hooke 1975). The current over the bar head diminishes, which enables filling to occur further upstream on the point bar margin (McGowen & Garner 1970; Pyrce & Ashmore 2005).

A number of essential studies focusing on meander dynamics date back to the 1970s and 1980s and are based on sparsely scattered, cross-sectional measurements of topography and flow (Table 1). Terrestrial (TLS) and mobile (MLS) laser scanning approaches, Acoustic Doppler Current Profiler (ADCP), and computational fluid dynamics (CFD) have later allowed for more detailed and temporally extensive analyses of the fluvio-morphological processes (cf. Ferguson *et al.* 2003; Heritage & Milan 2009; Hodge *et al.* 2009; Zinke *et al.* 2010; Alho *et al.* 2011; Jamieson *et al.* 2011; Vaaja *et al.* 2011). Even though various studies dealing with meandering (e.g. Ferguson *et al.* 2003; Frothingham & Rhoads 2003; Alho & Mäkinen 2010; Gautier *et al.* 2010; Termini & Piraino 2011; Engel & Rhoads 2012) have been undertaken recently, the fluvio-morphological processes on the point bar during a flood are not adequately documented using the available spatial and temporal resolution (see Pittaluga & Seminara (2011) for review in meander dynamic studies). In particular, the temporal occurrence of the erosion and deposition in relation to flow conditions has hardly been studied. It is not clear, for example, to which extent the bed configuration is formed during the flood peak and what the key factors leading to net erosion or deposition on different parts of the point bar are.

This study aims at giving new insights into these fluvio-morphological processes. The morphological changes, flow conditions, and their relationship on a meander point bar during a flood event are investigated. The morphological method (cf. Carson & Griffiths 1989; Bransington *et al.* 2003; Frothingham & Rhoads 2003; Gautier *et al.* 2010) is applied to determine the morphological changes on the point bar during one flood event; the detailed pre- and post-flood geometries of the point bar are surveyed using TLS and MLS. Flow velocity and direction, depth, and stream power are simulated using two-dimensional (2-D) CFD over the whole flooding period. In addition, the grain size distribution over the point bar is analyzed before and after the flood. Thus, this study investigates the distribution of fluvio-morphological processes on a point bar with a better spatial and temporal resolution than in any previous study.

STUDY AREA

The study was conducted in Northern Finland on the subarctic, meandering, Pulmanki River (Figure 1). The river channel has been eroded in the Pulmanki valley, where tens of meters of glacio-fluvial material has been deposited during the retreat of the continental ice (Mansikkaniemi & Mäki 1990). The channel is mobile and its banks are sensitive to erosion; the channel and point bars are unvegetated. An annual spring flood occurs due to snow melt in May and the ice-free period lasts from May to October. The seasonal discharge ranges from 4 to 50 $m^3 s^{-1}$ so that the typical spring flood discharge is ~40–50 $m^3 s^{-1}$, decreasing to 4–10 $m^3 s^{-1}$ by the middle of June. Normally, no other flood peaks occur that are comparable to the spring flood. The point bars are, thus, inundated by flood only at the spring time. Sediment transport is dominated by sandy bed load. The bed load transport rate on the study reach varies approximately between 0.04 and 0.1 $kg m^{-1} s^{-1}$. The D50 and D90 of the bed load vary between 0.1 and 1.4 and 0.3 and 3.7 mm, respectively. Grains up to 16 mm diameter are transported as bed load. The amount of suspended material at the rising flood stage is 180–280 $mg L^{-1}$. As the discharge drops, the fraction of bed load increases relative to total load. The mean gradient at the study reach is 0.2%.

Table 1 | Important field studies of meandering and point bar on a small and medium spatial and temporal scale. Sin. refers to sinuosity, width is in meters, and discharge (Q) is in $m^3 s^{-1}$. DEM refers to digital elevation model; ADV refers to Acoustic Doppler Velocimeter

Study	Focus	Study area	Sin.	Width	W/D	Q	Sediment	Topographic survey	Flow survey
McGowen & Garner (1970)	Physiographic features of point bars	Amite River, Louisiana: 2 point bars (Some observations also on Colorado River, reach of 260 km)	1.5	130	44	140	Sand to cobbles	Depth measurements Sedimentological observations	Discharge rating curves
Bridge & Jarvis (1976)	Flow and sedimentary processes in meander	The River South Esk Glen Clova, Scotland 1 simple meander bend	1.1	25	12	22 (b–f)	Sand & gravel	Echo sounding measurements 8 cross sectional profiles	Current meter 2 velocity profiles 3 survey campaigns
Bathurst *et al.* (1979)	Secondary flow and shear stress in river bends	River Severn Wales 4 meander bends	2–5	15	16–50	1–16	Gravel & cobbles		Electromagnetic flow meter Survey at bend apices, especially outer bank cells
Dietrich & Smith (1983)	Flow through a meander	Muddy Creek Platte County, Wyoming, USA 1 simple meander bend	1.8	6	11	1	Sand to granules	Cross sectional measurements	Current meter 9 velocity profiles 3 survey campaigns
Dietrich & Smith (1984)	Bedload transport in a meander	Muddy Creek Platte County, Wyoming, USA. 1 simple meander bend	1.8	6	11	1	Sand to granules	Dune size measurements using a meter stick	8 days, steady flow
Thompson (1986)	Secondary flow structures in meander bend	Skirden Beck, northwest England 2 successive bends	1.4	12	6.6	19 (b–f)	Gravel	Long term and short term morphological changes	Streamers Cross sectional survey Steady flow
Ferguson *et al.* (2003)	Flow structure in meander bends inner bank recirculation	River Dean, Cheshire plain northern England 2 natural meander bends	1.3	4.5	3	2	Sand & gravel	Total station, in total 404 points DEM building using kriging, one survey	3-D CFD, steady flow ADV (boundary, validation)

(*continued*)

Table 1 | continued

Study	Focus	Study area	Sin.	Width	W/D	Q	Sediment	Topographic survey	Flow survey
Frothingham & Rhoads (2003)	Flow structure and channel change in compound meander Channel and floodplain sediment dynamics, sediment load	Upper Embarras river Champaign county, Illinois, USA 1 compound meander bend	2.3	13–18	9	2	Sand & gravel	3 survey campaigns during 2 years One campaign took 2 days to execute	Three ADV campaigns 14 transects
Gautier *et al.* (2010)		Rio Beni, tributary of Rio Madeira Bolivian Amazonia 1 simple meander bend	2.9	550	40	2,000	Silt & sand	Echo sounding, RTK–GPS, total station DEM using kriging 4 survey campaigns	Discharge & water level Daily over 3 years
Engel & Rhoads (2012)	Interaction of flow and morphology; outer bank failures	Upper Embarras river Champaign county, Illinois, USA 1 compound meander bend	1.6	13–18	9	2	Sand & gravel	Total station and RTK–GPS: 6–8 transects per campaign 11 years, 12 surveys	ADV cross sections 2 surveys
Current study	Temporal occurrence of fluvio-morphological processes on point bar	Pulmanki river, tributary of Tana river northern Finland 1 simple meander bend	1.4	50–70	13	7–41	Sand to fine gravel	TLS and MLS 2700–7,200 points/m²	2-D CFD over one flood ADCP (boundary, validation) Unsteady flow

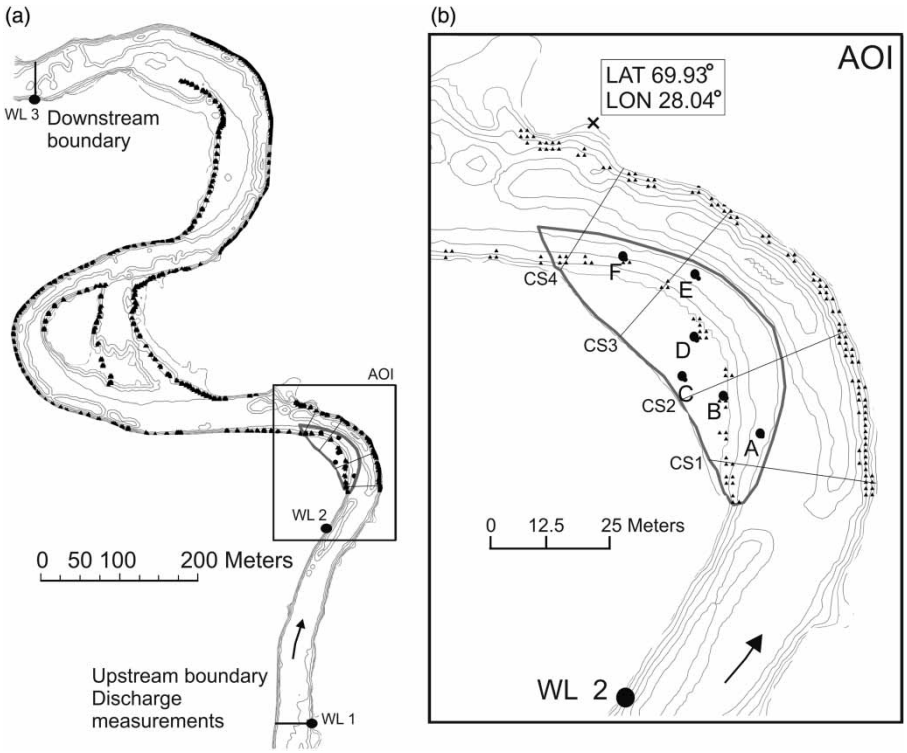

Figure 1 | (a) The reach of 2-D flow simulation along the Pulmanki River. The locations of water level record stations (WL 1–3), discharge measurements, and verification GPS measurements (black triangles) are marked in the figure. Records of WL 1 and WL 2 provided boundary data and WL 2 calibration data. (b) Area of interest. The area of the LiDAR survey is bordered by a grey thick line on the point bar. The points A–F represent locations where temporal variation of hydraulic parameters is analyzed. Cross-sections 1–4 (named CS4–CS4) represent the locations of ADCP measurements for model validations and the diagrams of Figure 4.

This study focuses on a point bar of 3,200 m^2 in size on a low-sinuosity meander bend (Figure 1(b)), which is comparable to many previous studies of meandering (Table 1). The width-to-depth ratio at the bend apex is 14 at the bank-full stage. The concave bank of the bend is steep and, since it is above the average summer time water surface level, it is covered by bushes and small trees (~2 m in height), which bind the erodible material. Also, the point bar is bordered by bushes and trees on the convex bank. In 2009, with a discharge rate of 40.7 $m^3 s^{-1}$, the spring flood peak water level was 2.3 m higher than in summer, reaching the vegetation on the convex bank. The discharge was bank-full. After May 22nd, the discharge remained below 15 $m^3 s^{-1}$ (Figure 2). Thus, the year 2009 was hydrologically representative and hence, the morphological development of the point bar may be approached as a typical impact of a spring flood on the study reach.

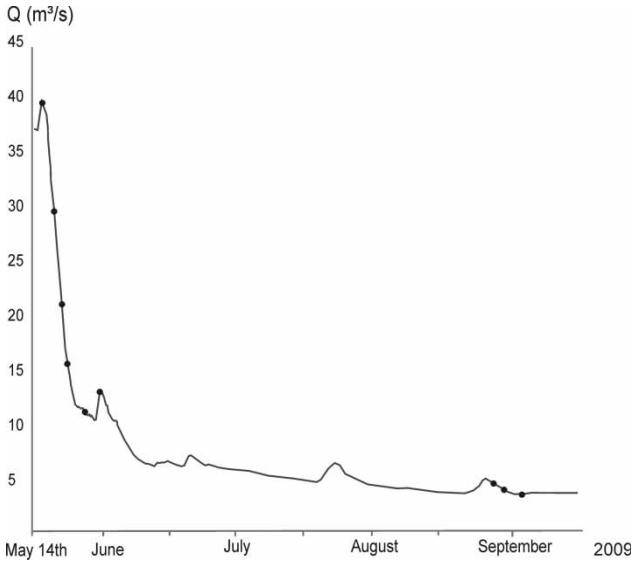

Figure 2 | Hydrograph of spring and summer 2009 on water level station WL 1 (see Figure 1 for location). The discharge was measured at nine different flow stages including flood and lower discharges. The times of discharge measurements are marked in the graph.

LASER DATA COLLECTION AND PROCESSING

TLS survey

The use of infra-red laser scanners requires a dry scanning target. Thus, the TLS and MLS surveys of the point bar were conducted during the low water stage: before the winter in 2008 and during the low summer flow of 2009. In total an area of 3,120 m^2 was scanned on the point bar. As the point bars are above the winter time water level, it was appropriate to realize the pre-flood laser scanning campaign before the winter. In the spring, the possible time frame for scanning is extremely short before the flood water rises. TLS (Leica HDS6000) was used to increase the point density of the MLS data of 2008 and to provide reference data for data verification and accuracy validation of both the 2008 and 2009 MLS campaigns. The data were acquired with a point spacing of 0.006 m at 10 m distance from the scanner. The TLS scan stations were positioned using VRS–GPS (Virtual Reference Stations–Global Positioning System) and predefined calibration offsets between the scanner origin and GPS antenna phase center were applied. Sphere target locations were measured using the VRS–GPS and the target center points were detected from the laser data. The scans were transformed to global coordinates (WGS84). The achieved precision of the point clouds was better than 0.01 m. The TLS scanning campaigns of 2009 and 2008 were performed in an identical manner.

MLS survey

Two MLS set-ups were used, i.e. a boat-based mobile mapping system (BoMMS) in 2008 and a cart-based mobile mapping system (CartMMS) in 2009 (Table 2). The MLS systems were composed of a LiDAR sensor and a navigation system, including GPS receivers and an IMU (inertial measurement unit). In the BoMMS, the LiDAR sensor was mounted on a 1.5 m-high stand mounted on an inflatable boat. A profile spacing of 0.1 m or less was achieved. In 2009, CartMMS was used to scan the point bar platforms. In both cases, the trajectory of the LiDAR sensor was post-calculated by integrating the observations of both the GPS (1 Hz) and IMU (100 Hz) to give a positional accuracy of 0.01 m. The MLS points were georeferenced in the same coordinate system with the TLS data.

Table 2 | Device details of the scanning campaigns

Campaign	Scanner	Scanning frequency (Hz)	Point frequency (kHz)
BoMMS (2008)	FARO LS 880HE80	15	120
CartMMS (2009)	FARO Photon80	30	120
TLS (2008)	Leica HDS6000		500
TLS (2009)	Leica HDS6000		500

The average point densities of TLS (~3,000 points/m^2) and BoMMS (~500 points/m^2) were lower than that of CartMMS (~7,400 points/m^2). Combining the BoMMS data with supplementary TLS point clouds from 2008, a point density of ~2,700 points/m^2 was achieved.

Accuracy assessment and DTM creation

The georeferenced MLS point clouds were filtered and the ground points were classified. The TLS point clouds that overlapped with the MLS data were used as reference data in the accuracy assessment. Clear systematic errors derived from GPS–IMU data were noted and removed from the BoMMS data set of 2008. Next, a triangulated irregular network (TIN) was derived from each MLS data set (BoMMS and CartMMS) for accuracy assessment. The accuracy was defined by subtracting the TIN models from the TLS point clouds. The derived quality parameters describing the *z*-values are presented in Table 3. The planimetric error of the MLS data was approximately 0.036 m.

Digital terrain models (DTMs) with 0.1×0.1 m cell size describing the point bar platforms in 2008 and 2009 were built on the basis of the TLS and MLS data. The 2008 DTM was built by combining the BoMMS and TLS point clouds of 2008. The 2009 DTM, meanwhile, was built on the basis of CartMMS data alone. The point clouds were thinned to have a point spacing of 0.1 m and the *z*-values were defined by calculating the average elevation from hits falling inside the grid cell of 0.1×0.1 m. A digital elevation

Table 3 | Accuracy of the *z*-value in MLS data sets: average error (Avg error), standard deviation of error (SDE) (in meters), root mean square error (RMSE), and minimum and maximum elevation errors (Min/Max dz)

	Avg error	SDE (σ)	RMSE	Min dz	Max dz
BoMMS (2008)	0.0196	0.0296	0.0288	–0.3	0.13
CartMMS (2009)	0.0317	0.0322	0.0404	–0.42	0.08

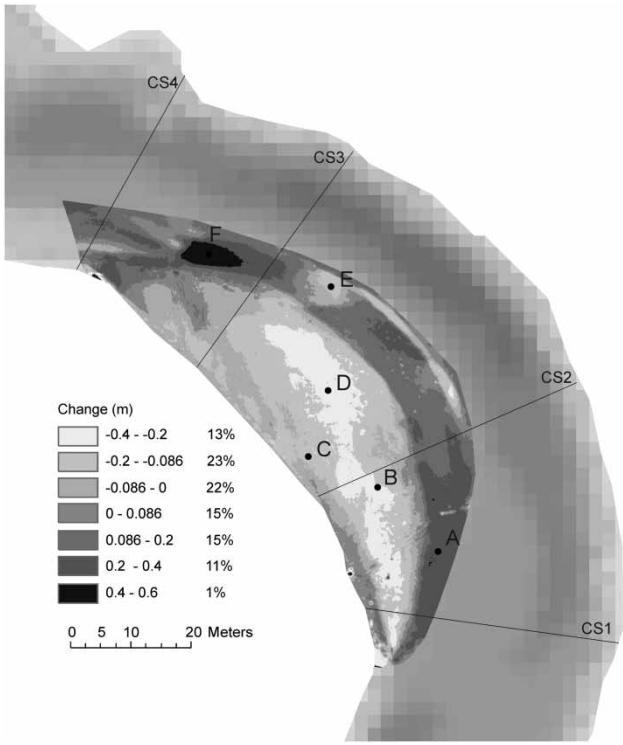

Figure 3 | Morphological changes on the point bar due to spring flood 2009. The observation points of hydraulic parameters and sediment size are marked in the figure. The fractional area of the point bar area experiencing changes of each class is presented in the legend in percent. The classes 0.086 to 0 and 0 to 0.086 are defined according to the specific LoD value, which determines the changes that are below the level of detail of the change detection. The channel is visualized in the background.

model of difference (DoD) with 0.1×0.1 m cell size was achieved by subtracting the 2008 and 2009 DTMs (see example in Figure 3).

Level of detail in change detection

To gain an insight into the accuracy of the calculated elevation change, an analysis determining uncertainties in the DoD model was carried out. The level of detection analysis (LoD) uses the standard deviation of error (SDE) of both DTMs and specifies the threshold LoD at a given confidence interval, as follows (cf. Milan *et al.* 2007):

$$U_{\text{crit}} = t((\sigma_1)^2 + (\sigma_2)^2)^{1/2} \quad (1)$$

where U_{crit} is the critical threshold error (i.e. threshold LoD) and t is the critical t-value at a chosen confidence level. If $t > 1(1\sigma)$, the confidence limit for change detection is 68%; if $t > 1.96$ (2σ), the confidence limit is equal to 95%. σ_1 and σ_2 are the SDEs of the BoMMS (2008) and CartMMS (2009) TIN models, respectively. The calculated LoD was 0.086 m with 95% confidence.

The LoD values represent the maximum level of detail in the change detection, since the LoD analysis was carried out using the MLS TIN models, even though the actual change detection was based on 0.1×0.1 m DTMs. In 2008, the DTM was constructed by combining TLS and MLS data, which improved the data resolution.

GRAIN SIZE DATA COLLECTION AND ANALYSIS

Sediment samples were collected from the point bar (points A–F in Figure 1(b)) before and after the flood. The pre-flood samples were collected in autumn 2008 and the post flood samples in summer 2009. The locations of the samples were measured using RTK–GPS (Real-Time Kinematic–GPS). The samples of approximately 0.5 kg in weight were taken from a layer of 0.03 m on the bar surface, after which they were dry sieved using a sieve interval of half phi. The D_{10}, D_{50} and D_{90} values of the samples were derived (Table 4).

Table 4 | Grain sizes (in mm) before (2008) and after (2009) the flood event. The sample locations (A–F) are marked in Figure 1(b) and Figures 3–5, and 6

	2008			2009		
	D10	D50	D90	D10	D50	D90
A	0.16	0.53	1.21	0.36	0.97	10.07
B	0.28	0.55	1.25	0.25	0.59	3.04
C	0.26	0.50	1.60	0.25	0.61	2.75
D	0.24	0.47	1.96	0.25	0.64	2.45
E	0.19	0.42	1.43	0.27	0.52	1.24
F	0.25	0.60	2.56	0.10	0.32	0.78

FLOW SIMULATION

Channel geometry

The bathymetry of the channel was surveyed by crossing the river at 2-m intervals using an echo sounder (FURUNO 5 FCV_600 L) mounted on an inflatable boat. The survey was conducted after the ice break in May 2009. The geometry of the bank-full channel was composed by combining the TLS and MLS and the echo sounding data (~0.5 points/m^2). A DTM with 2×2 m cell size was created using a kriging interpolation method.

Boundary, calibration, and verification data

To measure the water level variation during the entire ice-free period, water pressure sensors (Solinist Levelogger Gold Model 3001) were installed on the river bed at three locations before the flood peak (see Figure 1(b) for locations). The sensors measured the water depth at 15-minute intervals with 0.05% accuracy. The variation in water level was tied to a geographic coordinate system using RTK–GPS. The water surface elevation with respect to time was used as the downstream boundary condition. The water level record in the middle of the reach was used to calibrate the model.

Discharge was measured at the upstream boundary (see Figure 1(b) for location) using an ADCP (SonTek/YSI River Surveyor M9) during nine different discharges. The sensor consists of four 3 MHz and four 1 MHz velocity measurement transducers. The velocity measurement value is averaged from all eight beam pulses, having a recording frequency of 1 Hz. The accuracy of the flow measurement is ±0.25%. Discharge is calculated on the basis of the flow distribution in the cross section. A regression model converging the water level and discharge measurements on the upstream boundary was created and a discharge hydrograph was calculated based on the continuous water level record (Figure 2). The hydrograph was set as the upstream boundary condition.

Furthermore, the ADCP device was exploited to collect flow velocity profiles for model verification during the flood peak (May 16th) at water level station 2 and four cross-sections along the bend (see Figure 1(a) and (b) for locations). The shoreline of the river was mapped using RTK–GPS during a declining flood (May 20th) to verify the model.

Execution of simulation

The usage of CFD in natural river applications has increased notably during the last decade (cf. Booker *et al.* 2001; Rodriguez *et al.* 2004; Alho & Mäkinen 2010; Lotsari *et al.* 2010). The major advantages of CFD are good spatial and temporal resolution of flow field data. Even though three-dimensional (3-D) models predict the flow structure of curved channels most accurately (Lane *et al.* 1999), 2-D models are computationally more efficient and thus more applicable on natural river reaches. They have also shown to agreeably predict the flow field in a curved channel (e.g. Darby *et al.* 2002; Rodriguez *et al.* 2004; Alho & Mäkinen 2010). In addition, the requirements for field observations are modest compared to a 3-D model. Thus, a 2-D model was selected for this study. The simulation was carried out for a 2×2 m grid over the whole hydrograph (Figure 2) using a 2-D CFD, i.e. TUFLOW (Two dimensional Unsteady FLOW).

The model solves the Saint Venant depth-averaged 2-D shallow water equations (SWE). The 2-D SWE in the horizontal plane are described by the following partial differential equations for mass continuity (Equation (2)) and momentum conservation in the x (Equation (3)) and y (Equation (4)) directions for an in-plan Cartesian coordinate frame of reference.

$$\frac{\partial h}{\partial t} + \frac{\partial (Hu)}{\partial x} + \frac{\partial (Hv)}{\partial y} = 0 \tag{2}$$

$$\frac{\partial u}{\partial t} + \frac{u\partial u}{\partial x} + \frac{v\partial u}{\partial y} + c_f v + \frac{g\partial h}{\partial x} + gu\left(\frac{n^2}{H^{4/3}} + \frac{f}{2g\partial x}\right) * \sqrt{(u^2 + v^2)} - \mu\left(\frac{\partial^2 u}{\partial x^2} + \frac{\partial^2 u}{\partial y^2}\right) + \frac{\partial p}{\rho \partial x} = Fx \tag{3}$$

$$\frac{\partial v}{\partial t} + \frac{u\partial v}{\partial x} + \frac{v\partial v}{\partial y} + c_f u + \frac{g\partial h}{\partial y} + gv\left(\frac{n^2}{H^{4/3}} + \frac{f}{2g\partial y}\right) * \sqrt{(u^2 + v^2)} - \mu\left(\frac{\partial^2 v}{\partial x^2} + \frac{\partial^2 v}{\partial y^2}\right) + \frac{\partial p}{\rho \partial x} = Fy \tag{4}$$

where h is water surface elevation, t is time, g is gravitational acceleration, H is depth of water, u and v are depth averaged

velocity components in x and y directions, c_f is Coriolis force coefficient, n is Manning's n, μ is horizontal diffusion of momentum coefficient, f is form loss coefficient, ρ is density of water, p is atmospheric pressure, and Fx and Fy are the sum of components of external forces in x and y directions.

The model was calibrated by adjusting the surface roughness values (i.e. Manning's n value) and comparing the modeled and measured water surface elevation values at the mid-reach. The model was accepted when the difference was less than 0.05 m. The surface materials on the area were divided into four classes: channel, point bar, erosion protection, and forest – eventually yielding n-values of 0.028, 0.03, 0.045 and 0.05, respectively. The class 'erosion protection' was used over the concave banks of the two bends that are not investigated in this study, since they are covered by rip-rap erosion protections consisting of boulders with diameters of ~0.4 m. The model was run with a time step of 1.5, having a maximum of 10 iterations per event. After running the model, the simulation results were verified using the RTK–GPS data of the shoreline of the flood inundation on May 20th and the ADCP velocity profiles of the peak flood event (May 19th). The planar and horizontal difference between the modeled and measured shoreline location was less than 0.05 m on the studied bend. The simulated flow velocities were approximately 0.05–0.1 m s^{-1} lower than the ADCP-based measured depth-averaged velocities. Also, the depth-averaged flow directions along the bend agreed adequately with the ADCP measurements. The model was found to be operable.

Two flow occasions were extracted from the simulation results: the peak flood event (May 16th, $Q = 40.7$ m^3 s^{-1}, bank-full) and sharply decreasing flood event (May 19th, $Q = 28$ m^3 s^{-1}, 69% of the bank-full). The velocity values of four cross-sections along the bend were plotted as a diagram-presentation (see example, Figure 4).

In addition, 2-D map presentations were realized. The distribution of flow velocity and depth at bank-full flow and 69% of the bank-full flow were exported as point clouds with 2 m point spacing and processed using GIS software. They were interpolated into 2.5×2.5 m grids using a kriging method with a maximum of six points to calculate the value of one pixel. Contours representing depth with a 0.3 m interval were created from the depth information. Next, the distribution of stream power at the two flow

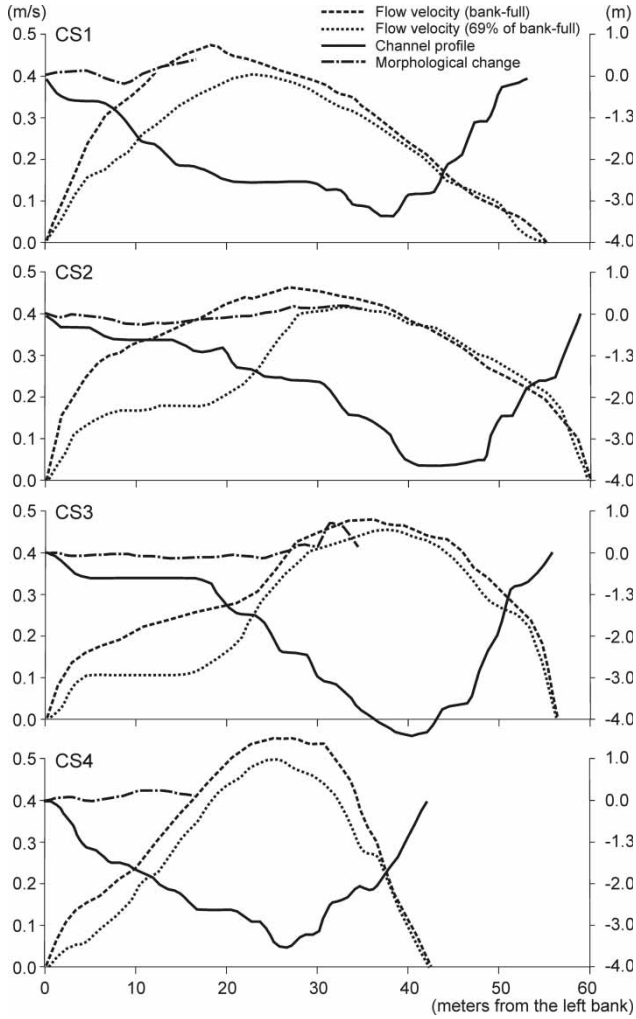

Figure 4 | Flow velocity at two different discharges (bank-full and 69% of bank-full), pre-flood channel profile and morphological change on the point bar at four cross-sections along the bend. The flow velocity values are shown on the primary axis and the channel profile and morphological changes on the secondary axes.

stages was calculated based on water surface slope, flow velocity, and depth as follows (Bull 1979):

$$\omega = \rho g H S v \tag{5}$$

where S is slope and v is velocity. The slope was defined based on the water level measurements. According to the water level measurements (WL1 and WL3), the water slope varied insignificantly during the flood and a constant value of 0.0015 was used. The resultant rasterized stream power distribution was visualized in parallel with the

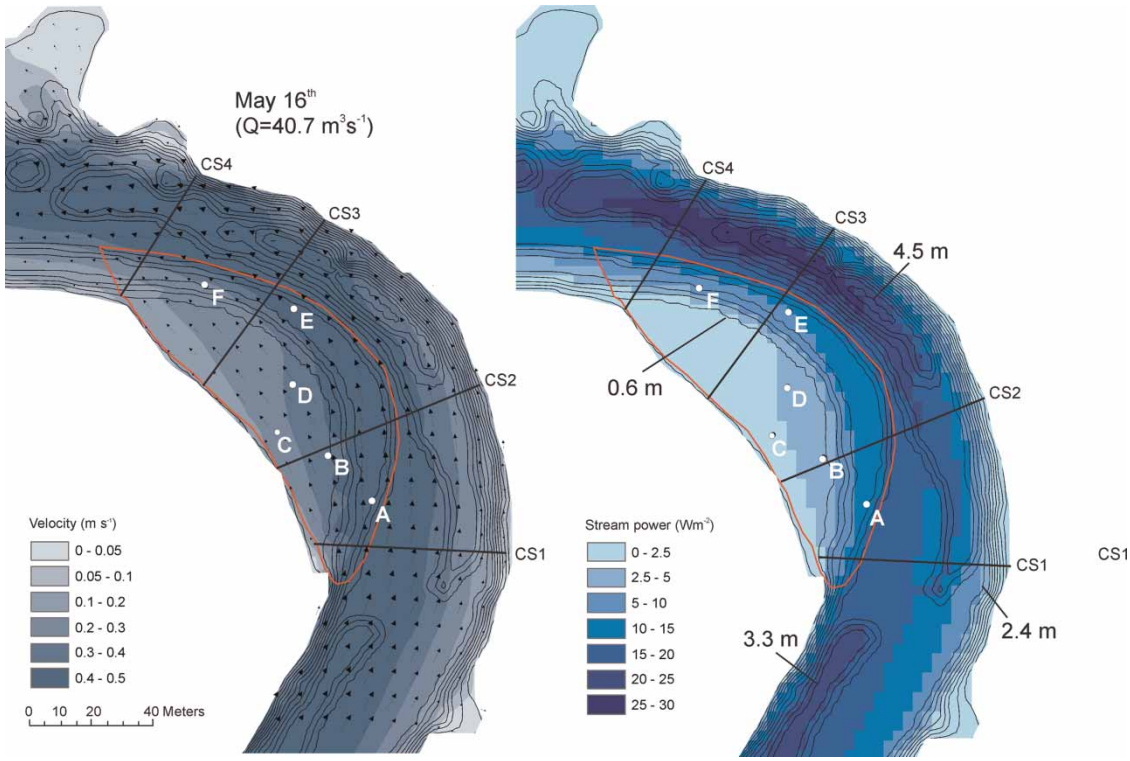

Figure 5 | Distribution of simulated depth (contours) and depth-averaged velocity and calculated stream power at bank-full stage. The depth contours have 0.3 m intervals and some depth values are marked in the figure. The arrows represent the depth-averaged flow direction. Note that the velocity and stream power class breaks are not linear. The cross-sectional lines along the bend represent the locations of the diagram plots of Figure 4 and the points A–E represent the observation points of Figure 7.

depth contours and flow vectors representing flow velocity and direction (see example, Figure 5).

Furthermore, the variation of depth, velocity, and stream power during the flood were plotted as a function of time at six locations on the point bar. The locations were selected to cover the most important parts of the point bar (see Figure 1).

RESULTS

Morphological changes on the point bar

Net erosion occurred on 56% of the point bar and 37% of the area showed elevation change values below the LoD; i.e. 0.086 m (with 95% confidence) (Figure 3). Seventy-five percent of the area experienced vertical changes of less than 0.2 m.

Net deposition occurred along the point bar margin as a longitudinal zone measuring ~8 m in width and a distinct scroll bar had evolved beyond the apex where up to 0.7 m of sediment had deposited (Figure 3, point F; Figure 4 CS3). A 0.2–0.4 m-thick layer of sediment had also deposited on the bar head margin (Figure 3, point A; Figure 4 CS1). The most significant area experiencing net erosion was the chute channel: a zone up to 25 m in width on the point bar platform (points B, C and D). This zone stretched up to the convex bank from mid bar to bar tail. In addition, erosion had occurred on the point bar margin, right beyond the apex (point E).

Flow velocity and stream power along the meander bend

The flow velocity along the bends is visualized as diagrams in Figure 4 and as 2-D map presentations in Figures 5 and 6 and stream power as 2-D map presentations in Figures 5 and 6. During bank-full discharge ($Q = 40.7\ m^3\ s^{-1}$), the HVC flowed over the bar head and was located on the point bar margin all the way until the tail (point F), shifting

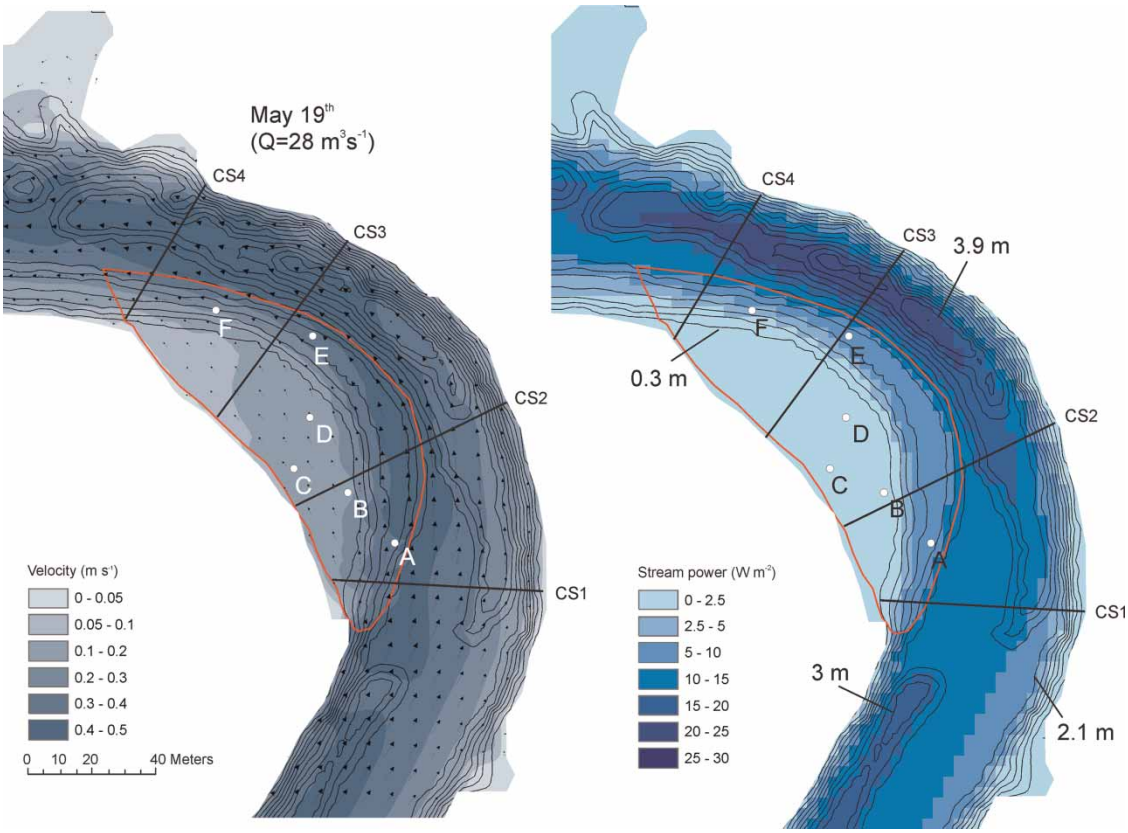

Figure 6 | Distribution of simulated depth and depth-averaged velocity and calculated stream power during decreasing discharge (69% of the bank-full). The depth contours have 0.3 m intervals and some depth values are marked in the figure. The arrows represent the depth-averaged flow direction. Note that the velocity and stream power class breaks are not linear. The cross-sectional lines along the bend represent the locations of the diagram plots of Figure 4 and the points A–E represent the observation points of Figure 7.

laterally outwards along the bend (Figures 4 and 5). Beyond the bend apex, the HVC was located on the proximity of the concave bank. The depth-averaged flow direction followed the main channel along the bar margin, the zone of net deposition, but at the point bar platform the flow was oriented straight across the bar downstream. The bar head deposition area and most of the bar margin experienced the highest flow velocities (0.4–0.5 m s^{-1}) and stream power (15 W m^{-2}) of the point bar area (Figure 4, CS 1; Figure 5). Over the scroll bar, the corresponding values were 0.2–0.3 m s^{-1} and ~7 W m^{-2}. When the flow passed the point bar top, the flow velocity and stream power diminished. Lower stream power (0–5 W m^{-2}) dominated the area of net erosion. However, the deepest erosion zone (points B and D) roughly followed a zone of moderate stream power (2.5–5 W m^{-2}) and the flow velocities were relatively high (0.3–0.4 m^3 s^{-1}) as the HVC crossed the point bar. In the main channel, the highest stream powers were 25–30 W m^{-2}. No flow separation at the inner bank was evident in the depth-averaged simulation results.

During the declining flood ($Q = 28$ m^3 s^{-1}), the HVC was still partly located on the point bar head on the upstream part of the bend, also shifting laterally towards the concave bank along the bend (Figures 4 and 6). The HVC had shifted away from the point bar around point E, thus, further upstream compared to the bank-full stage. Most of the point bar experienced flow velocities of less than 0.2 m^3 s^{-1}. On depositional zone on the bar margin, the flow velocity was 0.3–0.5 m s^{-1} and stream power was mostly below 10 W m^{-2}. Around the bar tail scroll bar, stream power was 2.5–5 W m^{-2}. On the point bar platform, the flow velocities were ~0.1–0.2 m^3 s^{-1} and stream power was less than 2.5 W m^{-2}. The flow directions were similar to bank-full stage. The highest stream power zone

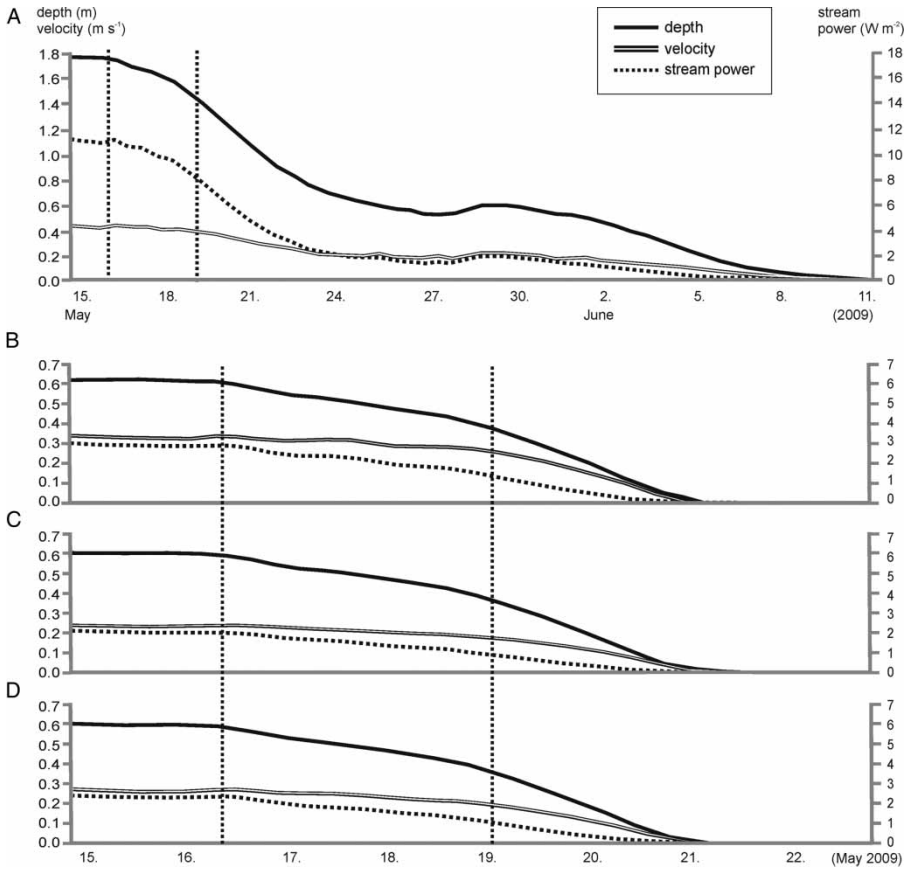

Figure 7 | The variation of depth, velocity, and stream power at observation points A–D (see locations in Figures 1, 3, and 4). Dates of the diagrams of Figure 4 and 2-D map visualizations of Figures 5 and 6 are marked with a vertical dotted line.

(20–25 W m^{-2}) was located close to the thalweg on the downstream part of the bend.

Temporal and spatial variation of hydraulic parameters and sediment size on the observation points

The variation of depth, stream power, and flow velocity were plotted as a function of time on the same observation points (Figures 7 and 8). Point A, located on the depositional area on the point bar head, was inundated for the longest time of all the points and experienced higher stream power compared to the other points during the bank-full discharge (max. 11 W m^{-2}) (Figure 7). Peak flow velocity was almost 0.5 m s^{-1} and the flow velocity was over 0.2 m s^{-1} for 18 days (until June 2nd). The flood depth halved by May 22nd. The increase in grain sizes was notable: the D_{50} increased from 0.53 to 0.97 mm and D_{90} from 1.21 to 10.07 mm (Table 4). After the flood, point A had the markedly largest grains of all observation points.

Point F, which lies on the scroll bar deposition beyond the bar apex, experienced notably weaker stream power compared to depositional point A; the maximum stream power was 6 W m^{-2} (Figure 8). The flood depth halved by May 22nd and the flow velocity was over 0.2 m s^{-1} for only 5–6 days. After that, the velocity remained between 0.1 and 0.2 m s^{-1} for 11 days. The grain size decreased and, after the flood, D_{10}, D_{50}, and D_{90} were smaller than on any other observation point (Table 4). The most substantial decrease occurred in the D_{90}, which diminished from 2.56 to 0.78 mm.

The hydrological conditions on point E on the bar margin were very similar to point A, although point E experienced net erosion (Figure 8). A maximum flow velocity of 0.5 m s^{-1} and a stream power of ~11 W m^{-2} were

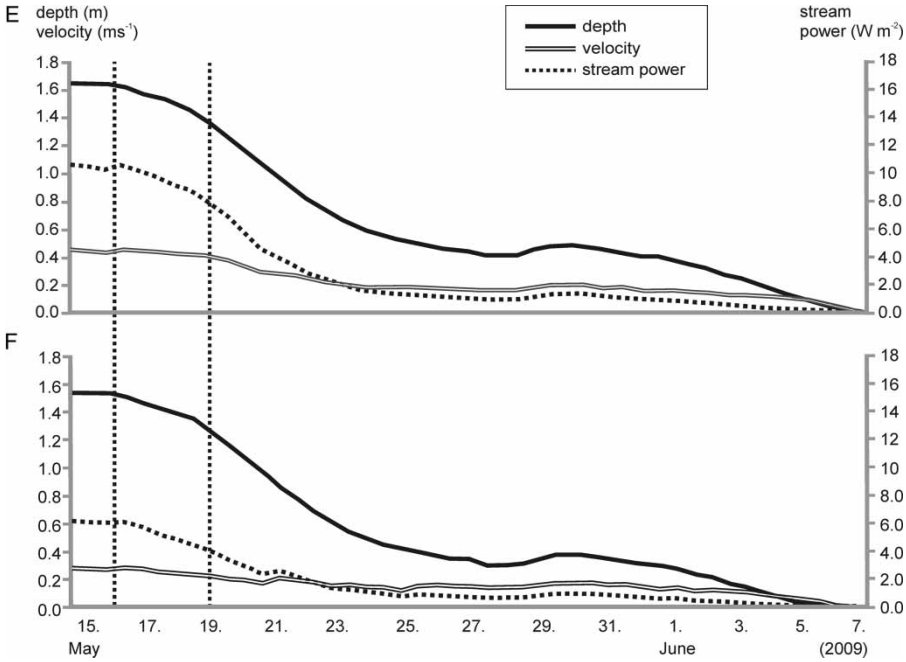

Figure 8 | The variation of depth, velocity and stream power at observation points E and F (see locations in Figures 1, 3, 5, and 6). Dates of the 2-D map visualizations (Figures 4 and 5) are marked with a vertical dotted line.

reached. The flow depth halved by May 22nd, as on point F. The flow velocity remained over 0.2 m s^{-1} for 8 days. After that, it was still over 0.1 m s^{-1} for ~13 days. The grain sizes did not show much change due to the flood; there was a small increase in D_{10} and D_{50} but a decrease in D_{90} (Table 4). Thus, especially after the flood, the grains were notably smaller than on point A.

The other observation points, i.e. B, C, and D, were located on the upper point bar on areas of net erosion. The stream power was low compared to depth at each point and the depth had diminished to half on May 19th (Figure 7). The inundated period was, as presumed, shorter than on the rest of the points, and the flood peak only caused a barely recognizable peak in stream power on May 16th. Point D lies on an area of most significant net erosion on the top of the point bar. However, stream power and flow velocity were higher on point B (3.0 W m^{-2} and 0.35 m s^{-1}) than on point D (2.4 W m^{-2} and 0.28 m s^{-1}) at peak flood. The flow velocities remained over 0.2 m s^{-1} for ~4 days on both points, slightly longer on point B than on point D. After that, the points were only inundated for 2 days. The grains on points B and D were rather similar to each other (D_{50} ~ 0.5–0.6 mm) (Table 4). The D_{50} and D_{90} values increased as a consequence of the flood; the increase was most notable in the D_{50} and D_{90} values at points D and B, respectively.

On point C, the peak stream power (2.1 W m^{-2}) and flow velocity (0.25 m s^{-1}) were lower than on points B and D. Flow velocity remained over 0.2 m s^{-1} for ~3 days. The area also experienced the lowest net erosion.

DISCUSSION

The 2-D simulation of this study coincided well with the field measurements and thus provided spatially and temporally extensive hydraulic data over a meander bend. Dietrich & Smith (1984) stated that the maximum sediment flux shifts according to the spatial distribution of stream power across the channel from near the inner bank in the upstream part of the bend towards the pool at the downstream part of the bend. However, as the spatial distribution of stream power varies depending on flow stage, the maximum sediment flux location also changes. Long-term studies of meander bends have also shown that, even though there is a high variability in the degree of activity among meander point bars, the bar

activity shows some relation to discharge events (Hooke 2007; Hooke & Yorke 2011). Our simulation indicated that the HVC and zone of high stream power were located closer to the concave bank at lower discharge compared to bank-full, during which the current flowed over the point bar head and hit the concave bank only beyond the apex; this is consistent with previous studies of meander bends (e.g. Hooke 1975; Ferguson *et al.* 2003). However, hardly any outward flow was evident over the upstream part of the point bar, according to the depth-averaged simulation, even though previous studies have shown that the outward flow should occur throughout the water column (Dietrich & Smith 1983). Even though 2-D simulations do not perform the lateral flow reliably in complicated environments (cf. Lane *et al.* 1999), it is clear that the outward flow did not occur throughout the water column in the simulation. Engel & Rhoads (2012) stated that the deflecting influence of the point bar to the flow field is essential for outward flow and the shift of HVC outwards. Thus, it seems that, during the flood, the discharge was too high to enable the deflection of flow by the point bar and to cause outward flow and such a strong HVC shift. Instead, the current straightened its way over the point bar during moderate discharge (69% of bank-full). In addition, the erosional zone over the point bar platform indicated that this current had eroded a chute channel across the point bar. Based on depth-averaged simulation, however, the flow velocity and stream power on the erosional zone was relatively low, reaching only 0.2–0.4 m s^{-1} and ~2–3 W m^{-2}, respectively, during bank-full flow. According to Kleinhans & van den Berg (2011), chutes do not form under specific stream power smaller than 10 W m^{-2} in sandy rivers ($D_{50} \sim 0.4$ mm). The sediment in Pulmanki was relatively fine, which is typical for the point bar platform (cf. Bridge & Jarvis 1976). According to Hjulström (1935)'s curve, the median-sized sediment in the area (~0.45–0.6 mm) required flow velocities over 0.2 m s^{-1} for net erosion to occur. McGowen & Garner (1970) found that accumulation of coarse grains is typical for chute filling and it occurs during decreasing discharge. According to our simulation, the flow velocities exceeded 0.2 m s^{-1} on the point bar platform for most of the inundated period, not leaving much time for chute filling. The grain sizes also increased in the area. The most notable increase in D_{90} occurred closer to the bar head, where the flow velocity was relatively high but net erosion was modest. It seems that the bar head part of the point bar platform in Pulmanki, despite the higher stream power compared to top of the point bar, experienced less erosion due to larger-grained sediment supply from upstream (cf. Lane *et al.* 1996), which settled down as chute fill at the end of the inundated period. Thus, the short duration of moderate flow velocities on the point bar platform left little time for chute filling and enabled erosion to dominate, even with relatively low stream power. Also Rinaldi & Darby (2008) have stated that the magnitude of fluvial erosion depends on the duration of the competent flow.

A local area of net erosion also occurred close to the bar margin, beyond the apex. The flow conditions were different and the area was inundated for ~15 days longer than the bar platform's erosional zone. The stream power was relatively high during bank-full flow. There was not much change in the flow velocities during the high discharges but, probably as a consequence of the HVC shift, the flow velocity experienced a drop around May 20th. Grain sizes before and after the flood were similar to each other ($D_{50} \sim 0.4$–0.5 mm), but the D_{90} value experienced decrease. It seems like most of the erosion occurred at the beginning of the inundated period, since, according to Hjulström (1935), over 0.2 m s^{-1} velocity was required to erode the median-sized grains (~0.5 mm) and this velocity was exceeded only for 8 days in the beginning of the flood. After that, the area was still inundated for 15 days. Dietrich & Smith (1984) have also reported that rolling of large grains towards the thalweg may complement net erosion on a steep point bar margin. According to the results of this study, the erosion on the bar margin, beyond the apex, similarly to the bar platform erosion, seems to be a consequence of the current over the bar head, which requires relatively high discharge to occur.

Deposition dominated the point bar margin otherwise, occurring most notably at the bar head and bar tail, consistent with the results of Pyrce & Ashmore (2005). Typically deposition is focused around the point bar margin beyond the apex (e.g. Bridge & Jarvis 1976; Gautier *et al.* 2010). According to some studies (e.g. McGowen & Garner 1970; Gautier *et al.* 2010), the bar head deposition detected on the Pulmanki reach is an untypical location for filling to occur on a point bar. As the stream power over the bar margin was relatively

high (~15 W m^{-2}) during bank-full flow, the analysis of the deposition over the bar head requires temporally extensive data. The flow conditions resembled the erosional area on the bar margin further downstream; it experienced high stream power and depth and a decrease in flow velocity as the HVC shifted outwards (around May 22nd). Thus, the reason why the area experienced deposition despite the high stream power probably lies in the shift in HVC and in the grain size distribution. The grains (especially D_{90}) were substantially larger on the bar head than on the margin further downstream, which is typical for point bars (Bluck 1982; Willis 1989; Bridge *et al.* 1995). The pre-flood median grains (D_{50} 0.53 mm) required a flow velocity of only 0.27 m s^{-1} to experience net erosion (Hjulström 1935); this was exceeded at the beginning of the flood for a period for 7 days. The median grain size increased during the flood, being 0.97 mm after the flood. The upper threshold velocity for deposition of post-flood D_{90} was 0.3 m s^{-1} and it was exceeded for only 7 days in the beginning of the flood. After that, the flow depth was still over 1 m and the area remained inundated for 21 days. The decrease in depth was notably faster during the beginning than during end part of the flood, and, as the increase in grain sizes in the area was notable, it seems like larger grains from upstream had settled in the area during the longer lasting medium discharges, this being the main reason for the filling. This conclusion also agrees with Pyrce & Ashmore (2005) who found that deposition occurs over the point bar head at low discharges.

The most notable depositional area on the point bar margin beyond the apex was a typical location for point bar accretion to occur, i.e. a scroll bar (cf. Gautier *et al.* 2010). The grain size distribution of the scroll bar area in Pulmanki resembled the erosional spot further upstream, but the flow conditions varied: flow velocity and stream power over the scroll bar were also low (0.3 m s^{-1} and 6 W m^{-2}) during the flood peak. According to McGowen & Garner (1970), the sudden increase in water depth past the top of the point bar decreases the flow velocity, enhancing filling on the downstream part of point bar. Grain sizes decreased notably as a consequence of the flood on the scroll bar (D_{50} from 0.60 to 0.32 mm), which is typical for slow-velocity zones (cf. Ashworth *et al.* 2000). According to Hjulström (1935), flow velocity of less than 0.05 m s^{-1} allows deposition of post-flood grains. According to the simulation, however, the velocity remained over 1 m s^{-1} almost for the entire inundated period, despite the relatively low peak flow velocity. The importance of secondary flow for inner bank deposition and scroll bar formation has been noticed in many previous studies (Dietrich & Smith 1984; Ferguson *et al.* 2003). In addition, the inward flow has been noticed to concentrate on the near-bed part of the water column (e.g. Bathurst *et al.* 1979; Frothingham & Rhoads 2003). The 2-D simulation, however, does not allow for consideration of the 3-D flow structure, a shortage that is emphasized on the downstream part of the point bar (Alho & Mäkinen 2010). This leads us to assume that the flow has been highly three-dimensional downstream part of the point bar and that the near-bed inward flow plays a key role in forming a scroll-bar.

Altogether, the results of this study agree well with the recent studies of Gautier *et al.* (2010) and Hooke & Yorke (2011) in that the point bar morphology itself has a major impact on the fluvio-morphological processes occurring over the bar. However, the spatial variability of the morphological changes seems to depend both on flood magnitude and duration, consistent with Middelkoop & Asselman (1998).

CONCLUSIONS

TLS and MLS data were used to detect the very detailed (sub-dm scale) changes that occurred during one flood event on a meander point bar. The flow characteristics over the whole flood event were simulated using 2-D CFD with unsteady flow. On the basis of the simulation and analyses, the following conclusions of the temporal distribution and key factors leading to erosion and deposition over the meander point bar can be drawn:

- The transverse shift of HVC towards the outer bank has a major impact on the point bar morphodynamics. The shift is, on the other hand, highly dependent on the point bar shape and discharge.
- As discharge decreases, the skew- and point bar-induced outward shift of HVC reduces the stream power experienced over the bar head, enabling filling to occur over the bar head during moderate and low discharges. The

filling is not only dependent on the decrease of flow velocity due to decreased discharge, but requires certain geometry of both the channel and the point bar.

- Deposition occurs mainly during the falling flood stage; thus, the duration of the moderate discharges has a major effect on the point bar accretion. In addition, an adequate supply of large grains from upstream will enhance the filling.
- The scroll bar formation is a consequence of the three-dimensional flow field and the 2-D CFD cannot describe the flow structure of the area, but will lead to incorrect assumptions of morphological changes on the point bar margin beyond the apex.
- Erosion on the point bar mainly takes place during high discharges, when the current over the point bar enables chute formation even with relatively low stream power, given that the material is not coarse. A fast decrease of discharge inhibits chute filling. Thus, in case the previous flood has deposited coarse material on the point bar platform, the scour may remain minor. Therefore, the magnitude of erosion is dependent on the past flood events more than on the depositional processes.
- Erosion may occur also on the bar margin beyond the apex given that the high-velocity current flows over the bar head. Thus, sufficiently high discharge and flow depth over the point bar are required and a steep bar slope may enhance the erosion.

This study has given insight to the fluvio-morphological processes on point bars with better spatial and temporal resolution than previous studies. However, to further improve understanding of the point bar fluvio-morphology, the flow structure should be considered using a 3-D CFD and the changes should be detected within the whole bend, not only on the point bar. In addition, sediment transport should be measured *in situ* to minimize the errors and deepen the analysis. Furthermore, the impact of snow and ice cover in the meander and point bar dynamics is an important future research subject. A study over several years would allow for the analysis of the consequences of duration of each discharge and river ice processes with greater reliability.

ACKNOWLEDGEMENTS

This study was funded by the Academy of Finland (RivCHANGE, RoadSide), TEKES (GIFLOOD), and by the Maj and Tor Nessling Foundation (FLOODAWARE). The TLS and MLS data were collected and processed by Mr Antero Kukko, and Mr Harri Kaartinen (Finnish Geodetic Institute). The field work was carried out with the assistance of Ms Eliisa Lotsari and Mr Claude Flener.

REFERENCES

Alho, P. & Mäkinen, J. 2010 Hydraulic parameter estimations of a 2-D model validated with sedimentological findings in the point bar environment. *Hydrol. Process.* **24**, 2578–2593.

Alho, P., Vaaja, M., Kukko, A., Kasvi, E., Kurkela, M., Hyyppä, J., Hyyppä, H. & Kaartinen, H. 2011 Mobile laser scanning in fluvial geomorphology: mapping and change detection of point bars. *Z. Geomorphol.* **55–2**, 31–50.

Ashworth, P. J., Best, J., Roden, J. E., Bristow, C. S. & Klaassen, G. J. 2000 Morphological evolution and dynamics of a large, sand braid-bar, Jamuna River, Bangladesh. *Sedimentology* **47**, 533–555.

Bathurst, J. C., Hey, R. D. & Thorne, C. R. 1979 Secondary flow and shear stress at river bends. *J. Hydr. Eng. Div.-ASCE* **105**, 1277–1295.

Bluck, B. J. 1982 Texture of gravel bars in braided stream. In: *Gravel-bed Rivers* (R. D. Hey, J. C. Bathurst & C. R. Thorne, eds). John Wiley & Sons, Chichester, pp. 339–355.

Booker, D. J., Sear, D. A. & Payne, A. J. 2001 Modelling three-dimensional flow structures and patterns of boundary shear stress in a natural pool-riffle sequence. *Earth Surf. Proc. Land.* **26**, 553–576.

Bransington, J., Langham, J. & Rumsby, B. 2003 Methodological sensitivity of morphometric estimates of coarse fluvial sediment transport. *Geomorphology* **53**, 299–316.

Bridge, J. S. & Jarvis, J. 1976 Flow and sedimentary processes in the meandering river South Esk, Glen Clova, Scotland. *Earth Surf. Proc.* **1**, 303–336.

Bridge, J. S., Alexander, J., Collier, R. E., Gawthrope, R. L. & Jarvis, J. 1995 Ground-penetrating radar and coring used to study the large-scale structure of point-bar deposits in three dimensions. *Sedimentology* **42**, 839–852.

Bull, W. B. 1979 Threshold of critical power in streams. *Geol. Soc. Am. Bull.* **90**, 453–464.

Carson, M. A. & Griffiths, G. A. 1989 Gravel transport in the braided Waimakariri River: mechanisms, measurements and predictions. *J. Hydrol.* **109**, 201–220.

Darby, S. E., Alabyan, A. M. & Van de Wiel, M. J. 2002 Numerical simulation of bank erosion and channel migration in meandering rivers. *Water Resour. Res.* **38**, 1163.

Dietrich, W. E. & Smith, J. D. 1983 Influence of the point bar on flow through curved channels. *Water Resour. Res.* **19**, 1173–1192.

Dietrich, W. E. & Smith, J. D. 1984 Bed load transport in a river meander. *Water Resour. Res.* **30**, 1355–1380.

Engel, F. L. & Rhoads, B. L. 2012 Interaction among mean flow, turbulence, bed morphology, bankfailures and channel planform in an evolving compound meander loop. *Geomorphology* **163–164**, 70–83.

Ferguson, R. I., Parsons, D. R., Lane, S. N. & Hardy, R. J. 2003 Flow in meander bends with recirculation at the inner bank. *Water Resour. Res.* **11**, 1322.

Friedkin, J. F. 1945 *A Laboratory Study of Meandering of Alluvial Rivers*. United States Waterways Experiment Station, Vicksburg.

Frothingham, K. M. & Rhoads, B. L. 2003 Three-dimensional flow structure and channel change in an asymmetrical compound meander, Embarras River, Illinois. *Earth Surf. Proc. Land.* **28**, 625–644.

Gautier, E., Brunstein, D., Vauchel, P., Jouanneau, J., Roulet, M., Garcia, C., Guyot, J. & Castro, M. 2010 Channel and floodplain sediment dynamics in a reach of the tropical meandering Rio Beni (Bolivian Amazonia). *Earth Surf. Proc. Land.* **35**, 1838–1853.

Heritage, G. L. & Milan, D. J. 2009 Terrestrial laser scanning of grain roughness in a gravel-bed river. *Geomorphology* **113**, 4–11.

Hjulström, F. 1935 Studies of the morphological activity of rivers as illustrated by the River Fyris, Upplasa. *B. Geol. I. Upps.* **25**, 221–527.

Hodge, R., Bransington, J. & Richards, K. 2009 Analysing laser-scanned digital terrain models of gravel bed surfaces: linking morphology to sediment transport processes and hydraulics. *Sedimentology* **56**, 2024–2043.

Hooke, R. 1975 Distribution of sediment transport and shear stress in a meander bend. *J. Geol.* **83**, 543–565.

Hooke, J. M. 2007 Spatial variability, mechanisms and propagation of change in an active meandering river. *Geomorphology* **84**, 277–296.

Hooke, J. M. & Yorke, L. 2011 Channel bar dynamics on multi-decadal timescales in an active meandering river. *Earth Surf. Proc. Land.* **36**, 1910–1928.

Jamieson, E. C., Rennie, C. D., Jacobson, R. B. & Townsend, R. D. 2011 Evaluation of ADCP apparent bed load velocity in a vlarge sand-bed river: moving versus stationary boat conditions . *J. Hydraul. Eng.-ASCE* **37**, 1064–1071.

Kleinhans, M. G. & van den Berg, J. H. 2011 River channel and bar patterns explained and predicted by an empirical and a physics-based method. *Earth Surf. Proc. Land.* **36**, 721–738.

Lane, S. N., Bradbrook, K. F., Richards, K. S., Biron, P. A. & Roy, A. G. 1999 The application of computational fluid dynamics to natural river channels: three-dimensional versus two-dimensional approaches. *Geomorphology* **29**, 1–20.

Lane, S. N., Richards, K. S. & Chandler, J. H. 1996 Discharge and sediment supply controls on erosion and deposition in a dynamic alluvial channel. *Geomorphology* **15**, 1–15.

Leopold, L. B. & Wolman, M. G. 1957 River channel patterns: braided, meandering and straight. *Geol. Surv. Prof. Pap.* **282–B**, 36–85.

Leopold, L. B. & Wolman, M. G. 1960 River meanders. *Geol. Soc. Am. Bull.* **71**, 769–794.

Lotsari, E., Veijalainen, N., Alho, P. & Käyhkö, J. 2010 Impact of climate change on future discharges and flow characteristics of the Tana River, Sub-arctic northern Fennoscandia. *Geogr. Ann. A.* **92**, 263–284.

Mansikkaniemi, H. & Mäki, O.-P. 1990 Paleochannels and recent changes in the Pulmankijoki valley, northern Lapland. *Fennia* **168** (2), 137–151.

McGowen, J. H. & Garner, L. E. 1970 Physiographic features and stratification types of coarse-grained point bars: modern and ancient examples. *Sedimentology* **14**, 77–111.

Middelkoop, H. & Asselman, N. E. M. 1998 Spatial variability of floodplain sedimentation at the event scale in the Rhine–Meuse delta, The Netherlands. *Earth. Surf. Proc. Land.* **23**, 561–573.

Milan, D. J., Heritage, G. L. & Hetherington, D. 2007 Application of a 3D laser scanner in the assessment of erosion and deposition volumes and channel change in a proglacial river. *Earth. Surf. Proc. Land.* **32**, 1657–1674.

Pittaluga, M. B. & Seminara, G. 2011 Nonlinearity and unsteadiness in river meandering: a review of progress in theory and modelling. *Earth Surf. Proc. Land.* **36**, 20–38.

Pyrce, R. & Ashmore, P. 2005 Bedload path length and point bar development in gravel-bed river models. *Sedimentology* **52**, 839–857.

Rinaldi, M. & Darby, S. E. 2008 Modelling river-bank-erosion processes and mass failure mechanisms: progress towards fully coupled simulations. In: *Gravel-bed Rivers VI: From Process Understanding to River Restoration* (H. Habersack, M. Piégay & M. Rinaldi, eds). Elsevier B.V., Oxford, UK, pp. 213–239.

Rodriguez, J. F., Bombardelli, F. A., Garcia, M. H., Frothingam, K. M., Rhoads, B. L. & Abad, J. D. 2004 High-resolution numerical simulation of flow through a highly sinuous river reach. *Water Resour. Manage.* **18**, 177–199.

Smith, C. E. 1998 Modeling high sinuosity meanders in a small flume. *Geomorphology* **25**, 19–30.

Termini, D. & Piraino, M. 2011 Experimental analysis of cross-sectional flow motion in a large amplitude meandering bend. *Earth Surf. Proc. Land.* **36**, 244–256.

Thompson, A. 1986 Secondary flows and the pool-riffle unit: a case study of the processes of meander development. *Earth Surf. Proc. Land.* **6**, 631–641.

Vaaja, M., Hyyppä, J., Kukko, A., Kaartinen, H., Hyyppä, H. & Alho, P. 2011 Mapping topography changes and elevation accuracies using a mobile laser scanner. *Remote Sens.* **3**, 587–600.

van den Berg, J. 1995 Predicting of alluvial channel patterns of perennial rivers. *Geomorphology* **12**, 259–279.

Willis, B. J. 1989 Palaeochannel reconstructions from point bar deposits: a three-dimensional perspective. *Sedimentology* **36**, 757–766.

Zinke, P., Reidar Boe Olsen, N. & Bogen, J. 2010 3D modelling of the flow distribution in the delta of Lake Øyeren, Norway. *Hydrol. Res.* **41**, 92–103.

First received 14 May 2012; accepted in revised form 20 November 2012. Available online 28 January 2013